

PolarBEVDet: Exploring Polar Representation for Multi-View 3D Object Detection in Bird's-Eye-View

Zichen Yu, Quanli Liu, *Member, IEEE*, Wei Wang, *Senior Member, IEEE*,
Liyong Zhang, *Member, IEEE*, and Xiaoguang Zhao

Abstract—Multi-view 3D object detection built upon the Lift-Splat-Shoot (LSS) mechanism provides an economical and deployment-friendly solution for autonomous driving. However, all existing LSS-based methods rely on transforming multi-view image features into a Cartesian Bird's-Eye-View (BEV) representation, neglecting the non-uniformity of the image information distribution, which results in loss information in the near and computational redundancy in the far. Furthermore, these methods struggle to exploit view symmetry, increasing the difficulty of representation learning. In this paper, to fundamentally remove these limitations, we propose to replace the Cartesian BEV representation with the polar BEV representation, which naturally adapts to the image information distribution and effortlessly preserves view symmetry by regular convolution. To achieve this, we elaborately tailor three modules: a polar view transformer to generate the polar BEV representation, a polar temporal fusion module for fusing historical polar BEV features and a polar detection head to predict the polar-parameterized representation of the object. In addition, we design a 2D auxiliary detection head and a spatial attention enhancement module to improve the quality of feature extraction in perspective view and BEV, respectively. Finally, we integrate the above improvements into a novel multi-view 3D object detector, PolarBEVDet. Experiments on nuScenes show that PolarBEVDet achieves superior performance, and the polar BEV representation can be seamlessly substituted into different LSS-based detectors with consistent performance improvement. The code is available at <https://github.com/Yzichen/PolarBEVDet.git>.

Index Terms—Multi-view 3D object detection, autonomous driving, Bird's-Eye-View, polar BEV representation

I. INTRODUCTION

MULTI-VIEW 3D object detection is a promising technology in the field of autonomous driving due to its low-cost deployment and rich semantic information [1]–[3]. Early attempts [4]–[8] approach this task primarily from the perspective of monocular 3D object detection, where 3D object detection is first performed for each view, and then the predictions from all views are fused through post-processing. While feasible, this detection scheme ignores information across views, resulting in sub-optimal performance.

Zichen Yu, Quanli Liu, Wei Wang and Liyong Zhang are with the School of Control Science and Engineering, Dalian University of Technology, Dalian 116024, China, and also with the Dalian Rail Transmit Intelligent Control and Intelligent Operation Technology Innovation Center, Dalian 116024, China (e-mail: yuzichen@mail.dlut.edu.cn; liuql@dlut.edu.cn; wangwei@dlut.edu.cn; zhly@dlut.edu.cn).

Xiaoguang Zhao is with the Dalian Rail Transmit Intelligent Control and Intelligent Operation Technology Innovation Center, Dalian 116024, China, and also with the Dalian Seasky Automation Co., Ltd, Dalian 116024, China (e-mail: xiaoguang.zhao@dlssa.com).

This work was supported in part by the National Natural Science Foundation of China under Grant 62373077 and in part by the Key Field Innovation Team Support Plan of Dalian, China, under Grant No.2021RT02. (Corresponding author: *Quanli Liu*).

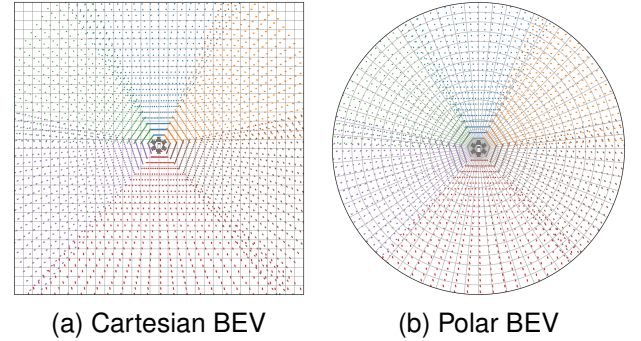


Fig. 1. Illustration of BEV grid distribution and image information distribution. The Cartesian BEV space is uniformly rasterized horizontally and vertically, and the polar BEV space is rasterized angularly and radially. The points with different colors represent the frustum points of the multi-view cameras carrying the image information, and their distribution is consistent with the polar grid distribution, which is dense in the near and sparse in the far.

Recently, many efforts [9]–[13] integrate cross-view information with the help of the Bird's-Eye-View (BEV), which removes inefficient fusion post-processing, and achieve significant advances in both detection performance and efficiency. In particular, the LSS-based paradigm utilizes the Lift-Splat-Shoot [14] mechanism to construct an explicitly dense BEV representation and has become one of the mainstream solutions. It is mainly composed of four modules: an image-view encoder for image feature extraction, a view transformer to transform image features from image-view to BEV by per-pixel categorical depth estimation, a BEV encoder composed of a series of 2D convolution blocks for further BEV feature extraction, and a detection head for 3D object detection in BEV space. In particular, the view transformer is pivotal to the whole framework, which bridges the gap between the image coordinate system and the Cartesian BEV coordinate system, integrating cross-view information into a unified Cartesian BEV representation. The Cartesian BEV representation is intuitive and traditional, but it suffers from the following two limitations: **1). The uniform grid distribution of the Cartesian BEV representation mismatches the non-uniform image information distribution.** As shown in Fig. 1(a), the nearby region contains richer and denser image information than the distant region, but the Cartesian BEV representation adopts the same grid granularity for all different distances. As a result, the grid distribution in the nearby region is too sparse for the rich information, leading to information loss. Conversely, the grid distribution in the distant region is too dense for the sparse information, causing computational redundancy. All existing

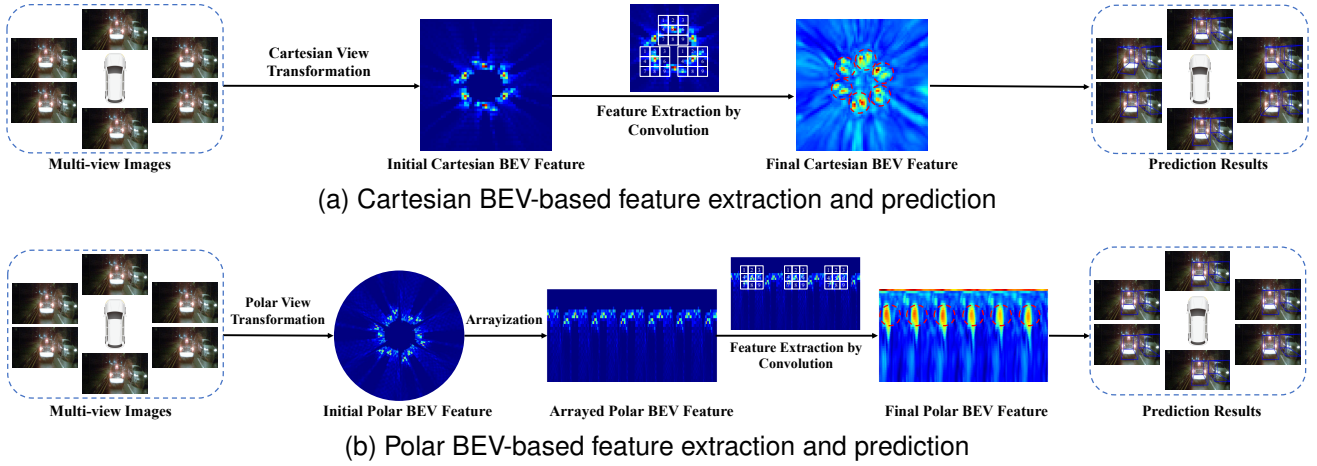


Fig. 2. Comparison of feature extraction and prediction based on different BEV representations. (a). Assuming that the multi-view cameras have the same imaging, the initial Cartesian BEV representation obtained by view transformation is view-symmetric. But the subsequent translation-invariant convolution operation destroys this symmetry, resulting in different object features and predictions at different azimuths. (b). When the polar BEV representation is employed, the object features are approximate and parallel in the arrayed polar BEV features. In this way, the view symmetry can be preserved using the regular convolution operation, leading to similar object features and predictions at different azimuths.

methods overlook this limitation because applying the uneven rasterization granularity to the Cartesian BEV space is challenging. 2). **The Cartesian BEV representation struggles to preserve the view symmetry of surround-view cameras during feature extraction.** As shown in Fig. 2(a), assuming that different cameras obtain the same object imaging, the input multi-view images are transformed into view-symmetric BEV features by the view transformation. But the subsequent translation-invariant regular 2D convolution operation destroys this symmetry during BEV feature extraction, which results in different object features being learned at different azimuths, increasing the difficulty of representation learning. AeDet [15] proposes an azimuth-equivariant convolution and an azimuth-equivariant anchor to model view symmetry property into the network, but it uses the customized convolution operator, which increases the complexity.

In this paper, we innovatively choose the polar BEV representation to replace the Cartesian representation. It rasterises the BEV space angularly and radially, eliminating the above limitations at the source: 1). **The grid distribution of the polar BEV representation is consistent with the distribution of image information, which is dense near and sparse far away as shown in Fig. 1(b).** Compared with the Cartesian BEV representation, the polar BEV representation naturally captures finer-grained information in the near region, while reducing computational redundancy in the far region. 2). **The polar BEV representation can conveniently preserve the view symmetry of surround-view cameras.** As shown in Fig. 2(b), in the polar BEV representation, features corresponding to the same object imaging from different views are parallel. Therefore, azimuth-equivalent object features can be extracted by simply performing regular 2D convolution operations.

However, switching to the polar BEV representation is non-trivial. To address this, we elaborately tailor three modules: a polar view transformer to generate the polar BEV representation, a polar temporal fusion module for fusing cached

historical polar BEV features and a polar detection head to predict the polar-parameterized representation of the object. Specifically, in the polar view transformer, we first lift the multi-view image features to the cylindrical coordinate system instead of the traditional Cartesian coordinate system, then the BEV space is rasterized angularly and radially, and finally the polar BEV representation is generated by BEV pooling. In the polar temporal fusion module, since ego-motion can be more conveniently formulated in the Cartesian coordinate system, we utilize the Cartesian coordinate as an intermediate proxy to align the multi-frame polar BEV features. In the polar detection head, we adopt polar parameterization for 3D object detection to exploit the preserved view symmetry, allowing the azimuth-equivalent prediction targets to be learned. Through the cooperation of these three modules, the Cartesian BEV representation is successfully replaced with the polar BEV representation.

In addition, the quality of image features in the perspective view is crucial for detection performance [16]–[19]. Many LSS-based works [11], [20], [21] introduce explicit depth supervision, which significantly enhances the depth-awareness of image features, but neglects the object-awareness. In this paper, we directly guide the network to learn the object-aware feature representation in the perspective view by introducing 2D auxiliary supervision. Specifically, we apply object classification supervision in the perspective view to improve the semantic discriminability of image features. To enhance the sensitivity of the network to object location, we additionally apply supervision on 2D object bounding box and center regression. It is worth noting that these 2D auxiliary tasks are active only during training, so they do not slow down inference.

Naturally, the feature extraction in the BEV space is also important. However, it is inevitable that a large amount of background noise exists in the BEV representation, which may interfere with the feature extraction for foreground objects. To mitigate the negative effects of background noise, we propose

a spatial attention enhancement (SAE) module consisting of two convolutional layers. It predicts a spatial attention weight map for weighting with the BEV feature map, guiding the network to focus on the foreground region while suppressing the background noise.

We integrate the above improvements to form a novel framework called PolarBEVDet. In summary, the main contributions of this paper are as follows:

- The polar BEV representation is proposed to replace the traditional Cartesian BEV representation for the LSS-based paradigm. It can mitigate the information loss in the nearby region and the computational redundancy in the far region, while also conveniently preserving the view-symmetry of multiple views.
- The 2D auxiliary supervision in perspective view is proposed for the LSS-based paradigm, which enhances the object-awareness of image feature representations.
- The spatial attention enhancement module is proposed to suppress the background noise and highlight the foreground information in BEV features, improving the quality of BEV representation.
- We evaluate the proposed PolarBEVDet on the challenging benchmark nuScenes [22]. Without any bells and whistles, our PolarBEVDet achieves remarkable detection performance (63.5% NDS and 55.8% mAP) on the nuScenes test split.

II. RELATED WORKS

A. Multi-view Camera-only 3D Object Detection

When dealing with multi-camera systems, previous works [4]–[7] utilize monocular 3D object detection to process each image separately, and then merge the detection results through post-processing in a unified coordinate system. This paradigm cannot simultaneously exploit the information from multi-view images and tends to miss truncated objects. Recent methods transform multi-view features from perspective view to a unified BEV representation for detection, which is not only convenient for the integration of multi-view information, but also more conducive to downstream tasks such as object tracking and trajectory prediction. In general, these methods can be roughly categorized into LSS-based and query-based methods.

1) *LSS-based methods*: As a pioneer of this paradigm, BEVDet [9] and BEVDet4D [10] follow the Lift-Splat-Shoot [14], which transforms the multi-view features into a dense BEV representation by predicting the categorical depth distribution for each pixel in the image feature map. BEVDepth [11] and BEVStereo [20] further introduce explicit depth supervision and stereo information to improve the quality of depth estimation. BEVPoolv2 [23] upgrades the view transformation process from the perspective of engineering optimization, significantly reducing computation and storage consumption. SA-BEV [24] proposes semantic-aware BEVPooling, which generates semantic-aware BEV features by filtering background information based on image semantic segmentation results. AeDet [15] proposes the azimuth-equivariant convolution and azimuth-equivariant anchor to preserve the radial symmetry properties of BEV features. To take

full advantage of the temporal information, SOLOFusion [21] utilizes both short-term, high-resolution and long-term, low-resolution temporal stereo. All of the above methods adopt the Cartesian BEV representation and ignore the object-awareness of image features. As far as we know, we are the first to explore the polar BEV representation and exploit 2D auxiliary supervision to improve the object-awareness of image features in the LSS-based paradigm.

2) *Query-based methods*: According to the meaning of query, query-based methods can be categorized into methods based on dense BEV query and sparse object query.

The dense BEV query-based methods generate a dense BEV representation with the help of a set of grid-shaped learnable BEV queries. Specifically, BEVFormer [12], BEVFormerV2 [16] utilize temporal self-attention and spatial cross-attention to efficiently aggregate spatial-temporal information from multi-view images and historical BEV features into BEV queries.

Inspired by Transformer-based 2D object detection [25]–[27], the sparse object query-based methods leverage object queries to represent 3D objects, and utilize the attention mechanism to aggregate features directly from multi-view images, thus avoiding explicit view transformation of image features. In particular, DETR3D [28] projects a set of 3D reference points generated by object queries into the multi-view images, and then samples the 2D features of the projection points to update the queries. However, this feature querying approach suffers from the problem of inadequate receptive fields. Therefore, PETR [13] and PETRv2 [29] propose the 3D position embedding to transform image features into 3D position-aware features, and then employ the global attention mechanism for the interaction between object queries and image features. Subsequently, VEDet [30], CAPE [31] and 3DPPE [2] improve the 3D position embedding of image features and achieve further performance improvement. StreamPETR [32] focuses on long temporal modeling to efficiently propagate long-term historical information through object queries, dramatically improving performance at negligible computational cost. To avoid computationally expensive global attention, SparseBEV [33] designs adaptive spatio-temporal sampling to generate sample locations guided by queries, and adaptive mixing to decode sampled features with dynamic weights from queries. While the query-based methods can achieve superior detection performance, they have higher localization errors and require greater deployment efforts than the LSS-based paradigm.

B. Polar-Based 3D Perception

1) *Polar-based 3D Lidar perception*: Due to the uneven distribution of lidar points in space and even long-tailed distribution, PolarNet [34] and Panoptic-PolarNet [35] propose a semantic segmentation and panoptic segmentation network for point clouds based on the polar BEV representation, respectively, which balances the number of points in each grid cell and indirectly aligns the attention of the segmentation network with the long-tailed distribution of points along the radial axis. However, these 3D-to-2D projection methods inevitably lose and change the 3D topology. Therefore,

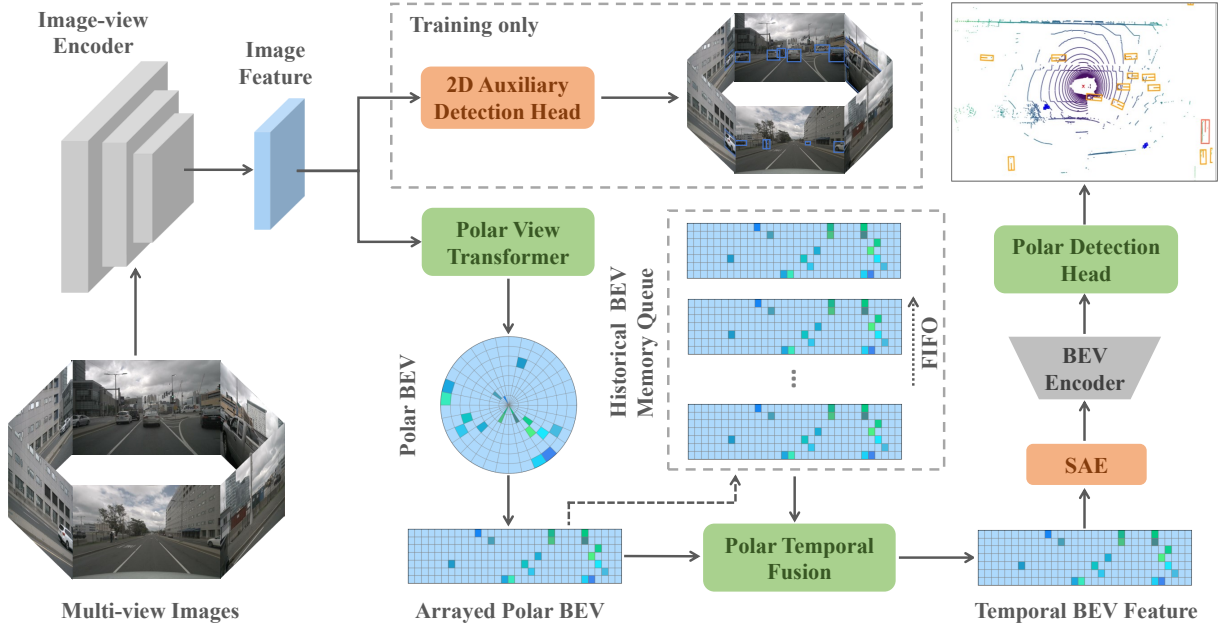


Fig. 3. Framework of PolarBEVDet. First, the multi-view image features extracted by the image-view encoder are fed to the polar view transformer to generate a polar BEV representation, which is subsequently arrayed to obtain an arrayed polar BEV representation. Then, the polar temporal fusion module fuses the cached historical polar BEV features to utilize the temporal information. Finally, the temporal BEV feature is sent to the polar detection head to predict the polar-parameterized representation of the object after further feature extraction by the SAE module and the BEV encoder. In addition, during the training phase, the 2D auxiliary detection head is applied to improve the feature quality in perspective view.

Cylinder3D [36] and DS-Net [37] resort to 3D cylindrical partition and asymmetrical 3D convolution networks for Lidar segmentation to better model the geometric information. When dealing with stream-based lidar perception, PolarStream [38] adopts the polar coordinate system instead of the Cartesian coordinate system to reduce computation and memory waste. For Lidar-based 3D object detection, in order to alleviate the feature distortion problem of the polar representation, PARTNER [39] designs a global representation re-alignment module consisting of dual attention and introduces instance-level geometric information into the detection head, achieving excellent performance beyond the Cartesian-based methods.

2) *Polar-based 3D vision perception*: PolarBEV [40] employs a height-based feature transformation to generate a polar BEV representation for BEV semantic segmentation and instance segmentation, where it adjusts the correspondence between BEV grids and image pixels by iteratively estimating the height of each polar grid. Extending from DETR3D [28], PolarDETR [41] proposes polar parameterization for 3D object detection, which establishes explicit associations between image patterns and predicted targets and exploits the view symmetry of the surround-view cameras. PolarFormer [42] transforms all image feature columns into a set of polar rays associated with learnable polar queries through the cross-attention mechanism [26], and these polar rays are subsequently aligned to generate multi-scale polar BEV maps for detection. These methods all build on the query-based paradigm, in contrast, we focus on the feasibility of polar BEV representation in the LSS-based paradigm and explore the capabilities (e.g., robustness and generalizability) of polar BEV representation in more depth.

III. METHOD

In this paper, we propose a novel multi-view 3D object detection framework, PolarBEVDet, in which we utilize the polar BEV representation instead of the Cartesian BEV representation commonly used in LSS-based methods. As shown in Fig. 3, we elaborately tailor three modules for the polar BEV representation: a polar view transformer for polar BEV representation generation, a polar temporal fusion module for fusing cached historical BEV features and a polar detection head for predicting the polar-parameterized representation of the object. Furthermore, we impose the 2D auxiliary supervision and the spatial attention enhancement module to improve the feature representation quality in perspective view and BEV, respectively. The image-view encoder and BEV encoder have no special design and simply follow the previous LSS-based methods [9], [11], [21].

A. Polar View Transformer

In the polar view transformer, we follow the LSS paradigm [14] to transform image features $F^{img} = \{F_k^{img} \in \mathbb{R}^{C \times H_F \times W_F}, k = 1, 2, \dots, N_{view}\}$ into a dense BEV feature for subsequent perception. Lift and Splat are two key steps in the LSS paradigm, which are used to lift the image features from 2D to 3D space and feature aggregation for generating the BEV feature map, respectively.

In the Lift step, we preset a set of discrete depths $\{d_0, d_1, \dots, d_{N_D-1}\}$ and utilize a depth estimation network to predict a depth distribution $D_k \in \mathbb{R}^{N_D \times H_F \times W_F}$ over these discrete depths for each image pixel. The frustum points $P_k \in \mathbb{R}^{3 \times N_D \times H_F \times W_F}$ and corresponding frustum features $F_k^{3D} \in \mathbb{R}^{C \times N_D \times H_F \times W_F}$ are derived for each image, where

the frustum features are obtained by scaling the image features with the predicted depth distribution. To obtain the polar BEV representation, we transform all the frustum points of each view into the cylindrical coordinate system instead of the Cartesian coordinate system. Specifically, given a frustum point $p = (u, v, d)$, it is first projected to a 3D point $p_{cart} = (x, y, z)$ in the Cartesian coordinate system according to the camera intrinsic and extrinsic:

$$[x, y, z, 1]^T = T^{-1}K^{-1}[u * d, v * d, d, 1]^T, \quad (1)$$

where $T \in \mathbb{R}^{4 \times 4}$ and $K \in \mathbb{R}^{4 \times 4}$ denote the extrinsic and intrinsic matrices. Then, the corresponding cylindrical coordinate $p_{cyl} = (\theta, r, z)$ is computed as follows:

$$\theta = \arctan2(y, x), \quad (2)$$

$$r = \sqrt{x^2 + y^2}. \quad (3)$$

In the Splat step, the BEV space is rasterized into a set of polar grids angularly and radially. The azimuth range $[-\pi, \pi]$ is uniformly divided into N_θ intervals with an interval of δ_θ , while the radial range $[r_{min}, r_{max}]$ is uniformly divided into N_r intervals with an interval of δ_r . The polar grid index (i, j) associated with each frustum point is then computed as follows:

$$i = \lfloor (\theta + \pi) / \delta_\theta \rfloor, \quad (4)$$

$$j = \lfloor (r - r_{min}) / \delta_r \rfloor. \quad (5)$$

The frustum features belonging to the same polar grid are aggregated by sum pooling [23] so that the 3D frustum features are splatted into a 2D polar BEV representation. Finally, to facilitate subsequent feature extraction via convolutional operations, we array this representation to obtain a regular feature map $F \in \mathbb{R}^{C \times N_\theta \times N_r}$.

B. Polar Temporal Fusion

Temporal information facilitates the detection of the occluded objects and can significantly improve the detection performance, especially the velocity prediction [21], [43]. In order to efficiently utilize the temporal information, we cache the polar BEV features from previous N_t timestamps in memory queue following [21]. When need ed, we align these historical features to the current timestamp for temporal fusion. This temporal alignment process involves determining the position of each element in the current polar BEV feature map within the historical feature map based on ego-motion, and then warping the historical features to the current coordinate system by bilinear interpolation.

However, describing the ego-motion in the polar coordinate system is challenging, whereas ego-motion can be succinctly and intuitively represented by a transformation matrix in the Cartesian coordinate system. Therefore, we use the Cartesian coordinates as an intermediate proxy for the alignment of multi-frame polar BEV features. As shown in Fig. 4, given a current polar BEV feature map $F_t \in \mathbb{R}^{C \times N_\theta \times N_r}$ and a previous polar BEV feature map $F_{t-1} \in \mathbb{R}^{C \times N_\theta \times N_r}$ (for

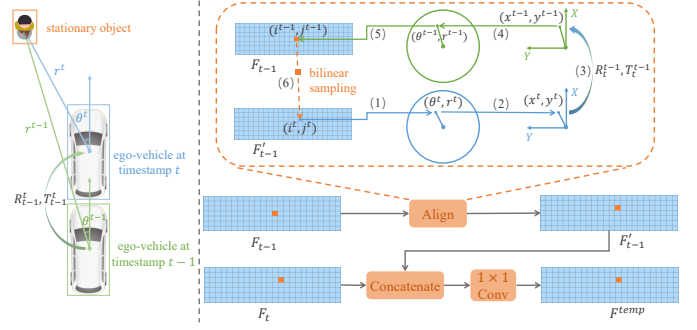


Fig. 4. Temporal fusion pipeline for polar BEV feature. The historical feature is aligned according to ego-motion and then fused with the current feature by concatenation and 1×1 convolution. The details of the temporal alignment is illustrated in orange dashed box. In addition, an example of a scenario is given on the left for ease of understanding.

simplicity, we use the case where $N_t = 1$ as an example), we compute the polar coordinate $p_p^t = (\theta^t, r^t)$ of the element at (i^t, j^t) in the current polar BEV feature map:

$$\theta^t = -\pi + i^t \times \delta_\theta, \quad (6)$$

$$r^t = r_{min} + j^t \times \delta_r. \quad (7)$$

The corresponding Cartesian coordinate $p_c^t = (x^t, y^t)$ is then computed for simplifying the coordinate transformation:

$$x^t = r^t \times \cos(\theta^t), \quad (8)$$

$$y^t = r^t \times \sin(\theta^t). \quad (9)$$

The ego-motion leads to a position shift of the objects in the feature map, even for stationary objects. Therefore, we compensate for this shift by inverse transformation, obtaining the position $p_c^{t-1} = (x^{t-1}, y^{t-1})$ of the current element in the previous Cartesian coordinate system as follows:

$$[x^{t-1}, y^{t-1}]^T = R_t^{t-1}[x^t, y^t]^T + T_t^{t-1}, \quad (10)$$

where $R_t^{t-1} \in \mathbb{R}^{2 \times 2}$ and $T_t^{t-1} \in \mathbb{R}^2$ represent the horizontal rotation and translation matrices of the ego-vehicle from timestamp t to timestamp $t-1$. Then we compute its coordinate $p_p^{t-1} = (\theta^{t-1}, r^{t-1})$ in the previous polar coordinate system and its position (i^{t-1}, j^{t-1}) in the feature map in turn. Finally, the aligned feature map F'_{t-1} at (i^t, j^t) can be obtained by:

$$F'_{t-1}(i^t, j^t) = \text{bilinear}(F_{t-1}, (i^{t-1}, j^{t-1})), \quad (11)$$

where $\text{bilinear}(F, P)$ denotes the bilinear interpolation of the point P in the feature map F , since (i^{t-1}, j^{t-1}) may not be a valid location in the feature map F_{t-1} .

The aligned BEV feature map F'_{t-1} is concatenated with the current BEV feature map F_t and then fused by the 1×1 convolution layers to generate the temporal polar BEV feature $F^{temp} \in \mathbb{R}^{C \times N_\theta \times N_r}$.

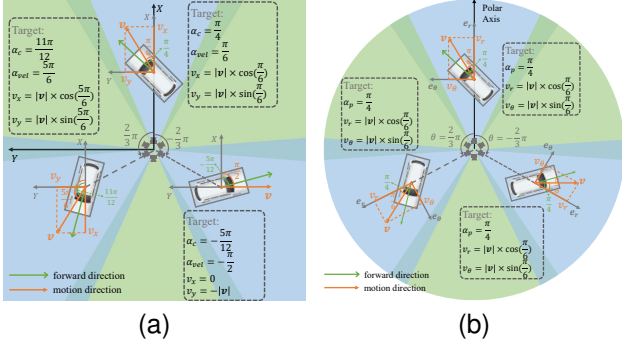


Fig. 5. Illustration of the Cartesian-parameterized and polar-parameterized prediction targets. Assume that multiple identical objects (represented by white cars) are distributed around the ego-vehicle, and that they are imaged identically in different views. (a) The Cartesian-parameterized prediction targets (for object orientation and velocity) are related to the azimuth of the object, which leads to the same imaging corresponding to different prediction targets. (b) In contrast, the polar-parameterized prediction targets are azimuth-equivalent, which reduces the optimization difficulty.

C. Polar Detection Head

We apply an anchor-free 3D object detection head following previous works [44] where the predicted target is the polar-parameterized representation of the object rather than the Cartesian-parameterized representation.

The original detection head contains a center heatmap branch and a group of attribute regression branches. The center heatmap branch outputs a 2D heatmap of K channels, each corresponding to one of the K object classes. It provides the object class and the rough location (c_x, c_y) of the object’s center in the Cartesian x-y plane. Meanwhile, the attribute regression branches utilize the center feature to predict the key attributes respectively: a sub-voxel center offset (o_x, o_y) to refine the center position, the object’s height z , the 3D dimensions (w, l, h) , the object’s orientation α_c and the velocity (v_x, v_y) along the Cartesian x-y axes.

However, the original detection head is built on the Cartesian BEV representation and parameterization, which is not compatible for our polar BEV representation. Moreover, as shown in Fig. 5(a), for the same imaging at different azimuths, it needs to regress different targets for the orientation and velocity of the object, inevitably increasing the prediction difficulty [15].

Therefore, for the polar BEV representation, we apply the polar parameterization to the object and tailor the polar detection head. In particular, the azimuth θ and radius r are used to describe the location of the object’s center. To determine them, we predict a heatmap to locate the rough position (c_θ, c_r) of the object’s center in the polar coordinate system and a center offset (o_θ, o_r) to compensate for the quantization error. For the orientation of the object, the conventional definition is the angle α_c between the object’s forward direction and the Cartesian x-axis. In order to effectively utilize the view symmetry property preserved by the polar BEV representation, we reformulate it as the angle α_p between the forward direction and the polar axis on which the object’s center is located as follows:

$$\alpha_p = \alpha_c - \theta. \quad (12)$$

Similarly, the original velocity is decomposed into velocity components (v_x, v_y) along the Cartesian x-axis and y-axis, respectively. We re-decompose it into radial velocity v_r and tangential velocity v_θ as prediction targets as follows:

$$v_r = |\mathbf{v}| \times \cos(\alpha_{vel} - \theta), \quad (13)$$

$$v_\theta = |\mathbf{v}| \times \sin(\alpha_{vel} - \theta). \quad (14)$$

where $|\mathbf{v}|$ is the magnitude of velocity and α_{vel} is the angle between the motion direction and the Cartesian x-axis. For the height and dimensions of the object, the original definition and prediction targets are retained. As shown in Fig. 5(b), the same imaging at different azimuths corresponds to azimuth-equivalent prediction targets by polar parameterization, which greatly eases the optimization difficulty.

As a result, the predicted object is represented as $(\theta = c_\theta + o_\theta, r = c_r + o_r, z, w, l, h, \alpha_p, v_\theta, v_r)$, which can be effortlessly converted back to the result of the Cartesian parameterization.

D. 2D Auxiliary Detection Head

In BEV perception system, the quality of image features in perspective view is crucial for the performance of 3D object detection [16], [17]. Ideally, image features should be depth-aware and object-aware. However, due to the existence of the view transformer, the final object detection in BEV space can only provide implicit and indirect supervision of these awareness capabilities [16]. This leads to confusing feature representation learning in the perspective view. Many LSS-based works [11], [20], [21] have introduced explicit depth supervision from LiDAR, remarkably improving the depth-awareness of image features, but neglecting the object-awareness.

In this paper, we directly guide the network to learn the object-aware feature representation in perspective view by introducing auxiliary 2D detection and corresponding supervision as follows:

1) *Classification*: The classification task aims to differentiate between object classes, including the background, car and pedestrian, etc.. By applying auxiliary classification supervision in the perspective view, image feature representations with higher semantic discriminability can be learned. Therefore, we attach a lightweight classification branch comprising two convolutional layers to the image features for predicting the confidence scores of the K object classes. During training, hungarian matching [25] is adopted for positive/negative sample assignment and the generalized focal loss [45] is used for classification supervision.

2) *Box Regression*: To enhance the network’s sensitivity to object position, we introduce an auxiliary supervision for 2D object detection in perspective view, which forces the network to learn more discriminative features for localization. These features are subsequently transformed into the BEV space to generate BEV representations with high position sensitivity, enabling more precise object localization. In parallel with the object classification branch, we attach another branch to predict the distance from the pixel position to the 4 sides of the bounding box following FCOS [46]. In the training phase, the

2D ground-truth bounding boxes are obtained by projecting the annotated 3D bounding boxes to the image, and L1 loss and GIoU [47] loss are used for regression supervision.

3) *Center Regression*: Object detection in BEV space is center-based, so the sensitivity to the object center is very crucial. Inspired by this, in order to further improve the precision of object localization, we introduce a center regression branch to predict the offset from the pixel position to the object center and supervise it with L1 loss. Besides, we further predict a center heatmap for locating the object center and supervise it with penalty-reduced focal loss [48]. The ground-truth center is the projection point of the 3D object’s center in the image.

E. Spatial Attention Enhancement

For 3D object detection task, it is necessary to focus more on the foreground information. However, it is inevitable that substantial background noise exists in the BEV feature representations, which may interfere with the feature extraction of foreground objects. To mitigate the negative impact of background noise, we propose a spatial attention enhancement (SAE) module. It improves the quality of BEV feature representation and detection performance by guiding the network to focus on the foreground regions while suppressing the background noise.

Given the extracted BEV feature map $F \in \mathbb{R}^{C \times N_\theta \times N_r}$, an attention weight map $M \in \mathbb{R}^{1 \times N_\theta \times N_r}$ is predicted by feeding it to a subnetwork Φ_s followed by a sigmoid function. Its expected values in the foreground and background regions are close to 1 and 0, respectively. By weighting the BEV features with it, the features in the foreground region are highlighted and the background noise is suppressed, enabling adaptive feature enhancement. Furthermore, to prevent incorrect information suppression and stabilize the training, a skip connection is employed. Finally, the enhanced BEV features $F' \in \mathbb{R}^{C \times N_\theta \times N_r}$ can be represented as:

$$F' = (1 + M)F, \quad M = \text{sigmoid}(\Phi_s(F)), \quad (15)$$

where the sub-network Φ_s consists of a 3×3 convolutional layer followed by batch normalization and ReLU activation, and concludes with a 1×1 convolutional layer for the final output.

IV. EXPERIMENTS

A. Datasets and Evaluation Metric

We evaluate our model on the nuScenes [22] dataset, which is a large-scale autonomous driving dataset containing sensor data from six cameras, one LiDAR, and five radars. This dataset consists of 1000 driving sequences and it is officially divided into 700/150/150 sequences for training/validation/testing, respectively. Each sequence lasts about 20 seconds, with a key sample selected every 0.5 seconds for annotation with 3D bounding boxes.

For 3D object detection, we measure the detection performance using officially provided evaluation metrics, including the mean Average Precision (mAP), nuScenes Detection Score (NDS), and five true positive (TP) metrics: mean Average Translation Error (mATE), mean Average Scale

Error (mASE), mean Average Orientation Error (mAOE), mean Average Velocity Error (mAVE), mean Average Attribute Error (mAAE). Among them, the mAP metric is used to measure the localization precision and it is calculated based on the center distance between the predicted and ground-truth objects in the bird’s eye view. The NDS is a comprehensive metric that combines mAP with all true positive metrics to provide a more holistic performance evaluation for 3D object detection.

B. Implementation Details

We accomplish the proposed improvement on the reimplemented SOLOFusion [21], in which single-task detection head replaces multi-task detection head to speed up the inference, and the 3D coordinate system is constructed by using the mean optical center of the multi-view cameras as the origin to substitute the lidar/ego coordinate system. During training, the image data augmentation and BEV data augmentation are applied following BEVDet [9]. PolarBEVDet is trained using the AdamW [51] optimizer with weight decay of $1e-7$ or $1e-2$. The learning rate is initialized to $1e-4$, and the batch size is set to 32.

When compared with other methods, we perform experiments with ResNet50 [52], ResNet101 [52] and V2-99 [53] backbones. The ResNet50 and ResNet101 backbones are initialized by ImageNet [54] and nuImages [22] pre-training, and the V2-99 backbone is initialized from the DD3D [5] checkpoint. The model is trained for 60 epochs for ResNet50 and ResNet101 without CBGS [55] strategy, and 36 epochs for V2-99 to prevent overfitting. For the ablation study, we utilized ResNet50 as the image backbone and the image size is 256×704 , and all experiments are trained for 24 epochs without using the CBGS [55] strategy. In addition, the default BEV resolution is 256×64 and is increased to 384×96 only when a large backbone(i.e. ResNet101, V2-99) is used.

C. Main Results

1) *nuScenes val split*: In Tab. I, we compare PolarBEVDet with previous state-of-the-art vision-based multi-view 3D detectors on the nuScenes validation split. When adopting ResNet50 [52] as the image backbone and the input size is 256×704 , PolarBEVDet outperforms the previous state-of-the-art LSS-based detector SOLOFusion [21] by a clear margin of 1.9% mAP and 2.1% NDS, and also outperforms the query-based detector SparseBEV [33] by 1.4% mAP and 1.0% NDS. By equipping the nuImages [22] pre-training, PolarBEVDet achieves a state-of-the-art performance of 56.7% NDS, which demonstrates its superior detection capability. Furthermore, by adopting ResNet101 [52] as the image backbone and scaling up the input size to 512×1408 , the performance of PolarBEVDet is remarkably improved and still outperforms other previous state-of-the-art detectors, which demonstrates the scalability of our proposed method for backbones with different capacities and varying input sizes.

2) *nuScenes test split*: In Tab. II, we report the performance comparison results on the test split, and it can be observed that PolarBEVDet achieves excellent detection performance.

TABLE I
PERFORMANCE COMPARISON ON THE NUSCENES VAL SPLIT. * BENEFITED FROM THE PERSPECTIVE-VIEW PRE-TRAINING

Method	Backbone	Input Size	NDS \uparrow	mAP \uparrow	mATE \downarrow	mASE \downarrow	mAOE \downarrow	mAVE \downarrow	mAAE \downarrow
BEVDepth [11]	ResNet50	256 \times 704	0.475	0.351	0.639	0.267	0.479	0.428	0.198
FB-BEV [49]	ResNet50	256 \times 704	0.498	0.378	0.620	0.273	0.444	0.374	0.200
AeDet [15]	ResNet50	256 \times 704	0.501	0.387	0.598	0.276	0.461	0.392	0.196
BEVPoolv2 [23]	ResNet50	256 \times 704	0.526	0.406	0.572	0.275	0.463	0.275	0.188
SOLOFusion [21]	ResNet50	256 \times 704	0.534	0.427	0.567	0.274	0.511	0.252	0.181
VideoBEV [50]	ResNet50	256 \times 704	0.535	0.422	0.564	0.276	0.440	0.286	0.198
StreamPETR [32]	ResNet50	256 \times 704	0.540	0.432	0.581	0.272	0.413	0.295	0.195
SparseBEV [33]	ResNet50	256 \times 704	0.545	0.432	0.606	0.274	0.387	0.251	0.186
PolarBEVDet	ResNet50	256 \times 704	0.553	0.450	0.529	0.275	0.465	0.256	0.199
StreamPETR* [32]	ResNet50	256 \times 704	0.550	0.450	0.613	0.267	0.413	0.265	0.196
SparseBEV* [33]	ResNet50	256 \times 704	0.558	0.448	0.581	0.271	0.373	0.247	0.190
PolarBEVDet*	ResNet50	256 \times 704	0.567	0.469	0.525	0.269	0.437	0.247	0.199
BEVDepth [11]	ResNet101	512 \times 1408	0.535	0.412	0.565	0.266	0.358	0.331	0.190
AeDet [15]	ResNet101	512 \times 1408	0.561	0.449	0.501	0.262	0.347	0.330	0.194
SOLOFusion [21]	ResNet101	512 \times 1408	0.582	0.483	0.503	0.264	0.381	0.246	0.207
SparseBEV* [33]	ResNet101	512 \times 1408	0.592	0.501	0.562	0.265	0.321	0.243	0.195
StreamPETR* [32]	ResNet101	512 \times 1408	0.592	0.504	0.569	0.262	0.315	0.257	0.199
PolarBEVDet*	ResNet101	512 \times 1408	0.602	0.508	0.478	0.264	0.350	0.231	0.203

TABLE II
PERFORMANCE COMPARISON ON THE NUSCENES TEST SPLIT. CONVNEXT-B [56] IS PRETRAINED ON IMAGENET [54], WHILE V2-99 [53] IS INITIALIZED FROM THE DD3D [5] CHECKPOINT. THE LISTED METHODS DO NOT USE FUTURE FRAMES DURING TRAINING OR TESTING

Method	Backbone	Input Size	NDS \uparrow	mAP \uparrow	mATE \downarrow	mASE \downarrow	mAOE \downarrow	mAVE \downarrow	mAAE \downarrow
BEVDepth [11]	V2-99	640 \times 1600	0.600	0.503	0.445	0.245	0.378	0.320	0.126
BEVStereo [20]	V2-99	640 \times 1600	0.610	0.525	0.431	0.246	0.358	0.357	0.138
AeDet [15]	ConvNeXt-B	640 \times 1600	0.620	0.531	0.439	0.247	0.344	0.292	0.130
SOLOFusion [21]	ConvNeXt-B	640 \times 1600	0.619	0.540	0.453	0.257	0.376	0.276	0.148
SA-BEV [24]	V2-99	640 \times 1600	0.624	0.533	0.430	0.241	0.338	0.282	0.139
FB-BEV [49]	V2-99	640 \times 1600	0.624	0.537	0.439	0.250	0.358	0.270	0.128
SparseBEV [33]	V2-99	640 \times 1600	0.627	0.543	0.502	0.244	0.324	0.251	0.126
VideoBEV [50]	ConvNeXt-B	640 \times 1600	0.629	0.554	0.457	0.249	0.381	0.266	0.132
PolarBEVDet	V2-99	640 \times 1600	0.635	0.558	0.429	0.253	0.389	0.247	0.127

Notably, PolarBEVDet outperforms SOLOFusion [21] with ConvNext-Base [56] backbone by 1.6% NDS and 1.8% mAP, even though we adopt a smaller V2-99 [53] backbone. In addition, compared to the query-based detector SparseBEV [33], PolarBEVDet significantly outperforms it by 1.5% mAP and 0.8% NDS and achieves 7.3% remarkably less mATE, demonstrating the effectiveness of our method and its superiority in object localization precision.

D. Ablation Studies

1) *Component analysis*: To analyze the impact of each component in PolarBEVDet, we report the overall ablation study in Tab. III. We take the reproduced SOLOFusion as the baseline, and then gradually add the polar representation, 2D auxiliary supervision, and the spatial feature enhancement module. By replacing the Cartesian BEV representation with the polar representation, the performance is boosted by 1.7% and 1.3% on mAP and NDS, respectively. Subsequently, by introducing 2D auxiliary supervision during training, a 1.5% mAP and 1.2% NDS improvement is observed without increasing the latency. Finally, we incorporate the spatial feature enhancement to emphasize the foreground information and

TABLE III
ABLATION OF DIFFERENT COMPONENTS IN POLARBEVDet. THE BASELINE IS SOLOFUSION [21] WITH AN INPUT RESOLUTION OF 256 \times 704, RESNET50 AS THE BACKBONE, AND A LONG-TERM HISTORY OF 16 FRAMES

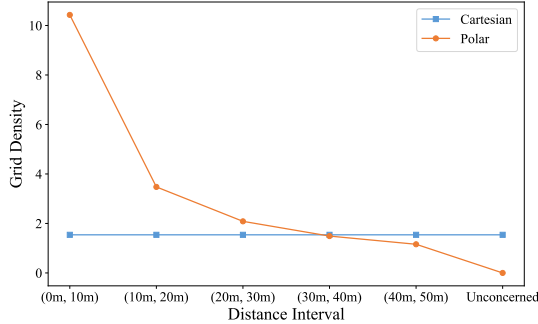
Baseline	Polar Representation	2D Auxiliary Supervision	SAE	NDS \uparrow	mAP \uparrow
✓	-	-	-	0.496	0.397
✓	✓	-	-	0.509	0.414
✓	✓	✓	-	0.521	0.429
✓	✓	✓	✓	0.527	0.434

suppress the noise, resulting in 0.5% mAP and 0.6% NDS improvement.

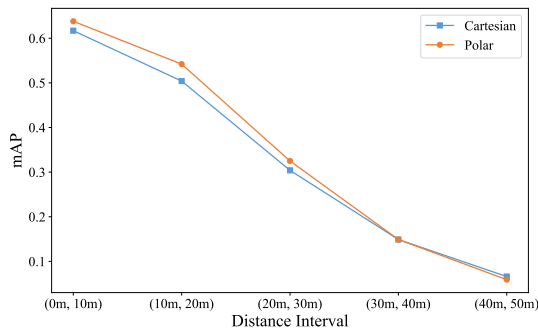
2) *Polar vs. Cartesian at different distances*: The Cartesian BEV and the polar BEV representation possess distinctly different grid distribution. In Fig. 6(a), we count the grid density corresponding to different distance intervals, which is defined as the number of grids contained per unit area. Notably, the Cartesian BEV representation has a resolution of 128 \times 128 while the polar BEV representation has a resolution of 256 \times 64, so the comparison is fair with the same amount of computation. It can be readily observed that the Cartesian

TABLE IV
PERFORMANCE OF CARTESIAN AND POLAR REPRESENTATIONS IN THE ORIGINAL VIEW AND REVOLVED VIEW

Representation	Original view	Revolved view	NDS \uparrow	mAP \uparrow	mATE \downarrow	mASE \downarrow	mAOE \downarrow	mAVE \downarrow	mAAE \downarrow
Cartesian	✓		0.496	0.397	0.613	0.295	0.660	0.265	0.192
		✓	0.472	0.383	0.643	0.300	0.729	0.323	0.198
Polar	✓		0.509	0.414	0.579	0.290	0.610	0.296	0.209
		✓	0.505	0.411	0.588	0.291	0.624	0.292	0.212



(a)



(b)

Fig. 6. Comparison of grid density and detection performance between Cartesian and polar BEV representations in different distance intervals. (a) The grid of Cartesian BEV representation is uniformly distributed, even in unconcerned regions. In contrast, the polar BEV representation has a grid distribution that is dense in the near and sparse in the far, and it can ignore the unconcerned regions. (b) The detection performance of the polar BEV representation is significantly better than that of the Cartesian BEV representation in the near region, while it is only slightly degraded in the far region.

representation has a uniform grid distribution, while the polar representation has a dense near and sparse far distribution. This suggests that with the polar BEV representation, the network’s attention is more focused on the near area. This is close to the way human drivers perceive, since human drivers also tend to focus and react more on things and situations in the near area.

In addition, we compare the perception performance of Cartesian and polar representations for different distance intervals. As shown in Fig. 6(b), in the range of 0 – 30 m, the polar BEV representation has a significant improvement on mAP, which indicates that the polar representation is more advantageous for the perception in nearby regions. While in the range of 40 – 50 m, there is a slight decrease in the detection performance of the polar BEV representation, which is due to the sparse grid distribution in the distant

regions. Nevertheless, this decline is acceptable because the polar representation significantly optimizes the perception of critical nearby areas, resulting in overall benefits and better aligning with the actual perception needs of driving.

3) *Polar vs. Cartesian on robustness to different azimuths:* When a vehicle turns at a large angle, the camera orientation changes significantly. To accurately detect surrounding objects under these conditions, the autonomous driving system must be robust to changes in azimuth. To reveal the effect of polar and Cartesian representations on the detection robustness to different azimuths, we follow AeDet [15] to perform the revolving test. Specifically, we rotate the vehicle 60 degrees clockwise and the original view [‘FRONT LEFT’, ‘FRONT’, ‘FRONT RIGHT’, ‘BACK RIGHT’, ‘BACK’, ‘BACK LEFT’] becomes the revolved view [‘BACK LEFT’, ‘FRONT LEFT’, ‘FRONT’, ‘FRONT RIGHT’, ‘BACK RIGHT’, ‘BACK’], and then we evaluate the detection performance of polar- and Cartesian-based detectors in the original view and the revolved view, respectively.

As shown in Tab. IV, for the Cartesian BEV representation, replacing the original view with the revolved view decreases the mAP and NDS by 1.4% and 2.4%, respectively, and the translation, orientation, and velocity errors also grow significantly. This suggests that the azimuth change has a significant adverse effect on the performance of the Cartesian-based detector. On the contrary, for the polar BEV representation, the detection performance in the rotated viewpoint is only slightly degraded, with mAP and NDS decreasing by only 0.3% and 0.4%. This suggests that the polar-based detector is more robust to azimuth changes, due to the fact that its feature learning and prediction targets are azimuth-independent.

TABLE V
COMPARISON OF LSS-BASED BASELINES AND CORRESPONDING POLAR VERSIONS. THE POLAR VERSIONS REPLACE THE CARTESIAN BEV REPRESENTATION IN BASELINES WITH THE POLAR BEV REPRESENTATION

Method	NDS \uparrow	mAP \uparrow	mATE \downarrow	mASE \downarrow	mAOE \downarrow	mAVE \downarrow	mAAE \downarrow
BEVDet [9]	0.360	0.279	0.774	0.286	0.659	0.827	0.247
+Polar	0.382	0.302	0.739	0.278	0.558	0.877	0.238
BEVDet4D [10]	0.426	0.299	0.767	0.285	0.608	0.374	0.198
+Polar	0.450	0.323	0.714	0.289	0.559	0.360	0.190
BEVDepth [11]	0.457	0.338	0.670	0.281	0.580	0.360	0.225
+Polar	0.474	0.352	0.656	0.282	0.526	0.369	0.193

4) *Generalization of the polar representation:* To verify the generalization and portability of the polar BEV representation, we port it to multiple LSS-based detectors and then evaluate the performance gain it brings. During porting, we

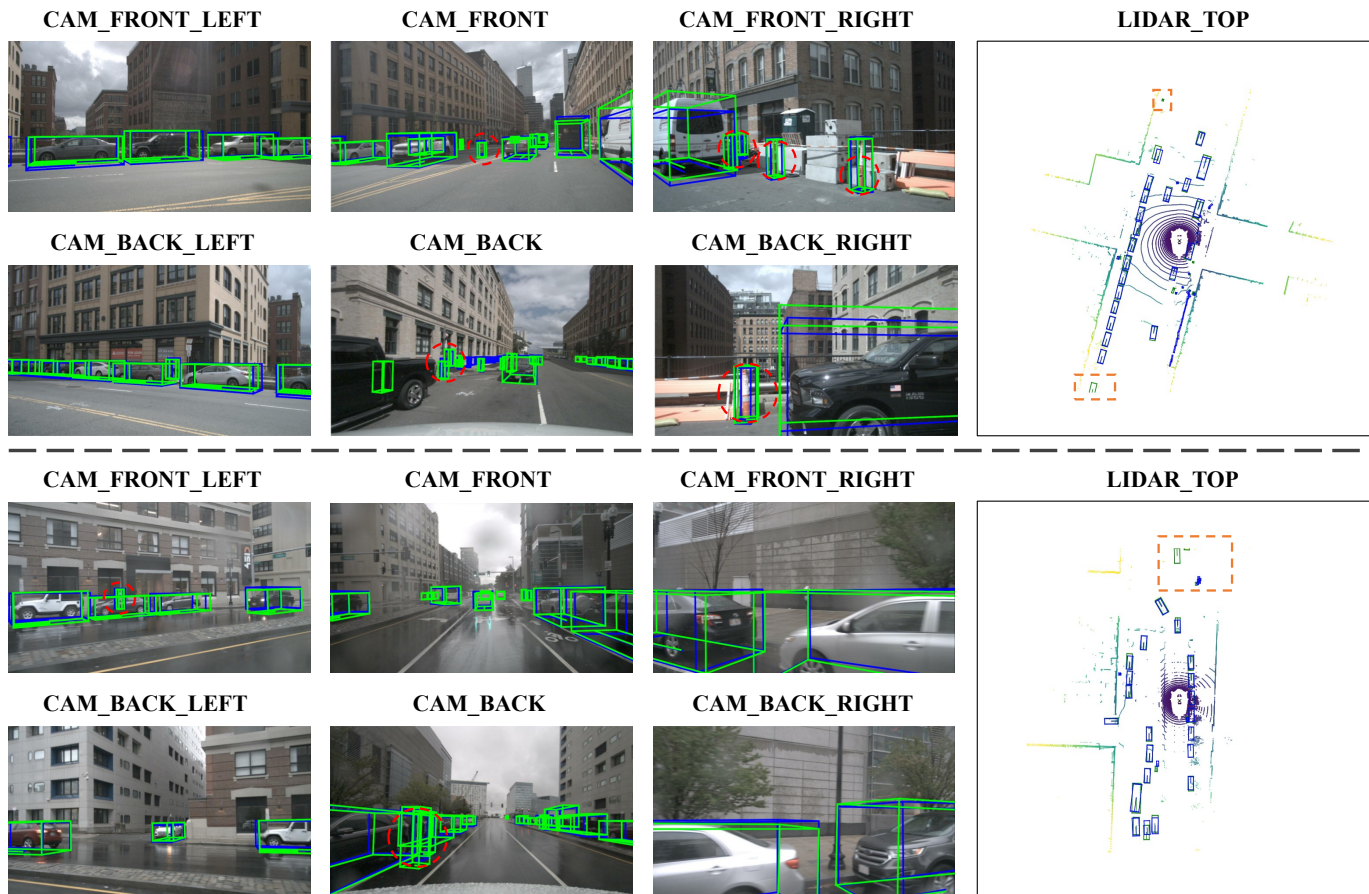


Fig. 7. Qualitative results of prediction results in perspective view and BEV. The predicted and ground-truth objects are denoted by blue and green boxes, respectively. In addition, some success cases of small object detection and failure cases of distant object detection are marked by red circles and orange rectangular boxes, respectively.

simply replace the original Cartesian-based modules with our designed polar view transformer, polar temporal fusion module and polar detection head for fair comparison.

We select BEVDet [9], BEVDet4D [10] and BEVDepth [11] as baselines and compare them with their corresponding polar versions as shown in Tab. V. The results show that both mAP and NDS of the polar versions obtain consistent improvements compared to the baselines, and the translation and orientation errors are significantly degraded. This demonstrates that the polar BEV representation has superior generalization ability across different models.

5) *Effect of 2D auxiliary supervision*: To further explore the role of each sub-task in 2D auxiliary supervision, we conduct an ablation study, as shown in Tab. VI. Starting with the baseline without 2D auxiliary supervision, the initial integration of box regression supervision to improve sensitivity to object’s location results in a 0.6% and 0.7% increase in mAP and NDS, respectively. Subsequently, we introduce classification supervision to improve the semantic discriminability of features, further increasing mAP by 0.5% and NDS by 0.4%. Finally, by incorporating center regression supervision to improve the sensitivity to the object’s center, our method achieves a 0.4% mAP and 0.2% NDS improvement. Overall, these 2D auxiliary supervision tasks can effectively improve

the detection performance by enhancing the quality of image features.

TABLE VI
ABLATION OF 2D AUXILIARY SUPERVISION. THE SUPERVISION OF BOX REGRESSION, CLASSIFICATION, AND CENTRAL REGRESSION IS ADDED SEQUENTIALLY

Setting	NDS \uparrow	mAP \uparrow
w/o 2D Supervision	0.514	0.419
+ Box Regression	0.521	0.425
+ Classification	0.525	0.430
+ Center Regression	0.527	0.434

6) *Effect of insertion position of SAE*: The optimal insertion location of the SAE module is difficult to determine directly, so we address this problem by comparing some potential insertion locations in Tab. VII. The results show that the detection performance is sensitive to the insertion location of the SAE module. Among all configurations, inserting the SAE module before the BEV encoder in configuration C is the optimal choice, achieving the highest 43.4% mAP and 52.1% NDS. In configuration B, when the SAE module is inserted before temporal fusion, mAP and NDS decrease by 0.5% and 0.4% compared to configuration A without SAE. This indicates that SAE negatively affects the temporal fusion since it may lead

to feature inconsistency of the object across frames. When we postpone the SAE module to the back of the BEV encoder in configuration D, mAP and NDS decrease by 0.4% and 0.2% compared to configuration C. This indicates that employing SAE before the BEV encoder to suppress background noise and emphasize foreground information is more conducive to BEV feature extraction.

TABLE VII
PERFORMANCE COMPARISON OF DIFFERENT INSERTION POSITIONS OF SAE

Configuration	Instertion Position	NDS \uparrow	mAP \uparrow
A	None	0.521	0.429
B	Before Temporal Fusion	0.517	0.424
C	Before BEV Encoder	0.527	0.434
D	After BEV Encoder	0.525	0.430

E. Qualitative Results

The qualitative detection results are shown in Fig. 7. The 3D bounding boxes are projected and drawn in BEV space and perspective views. We can observe that the predicted bounding boxes are close to the ground-truths even for small objects (e.g. traffic cones and pedestrians), proving the superior detection performance of PolarBEVDet. However, our method still has some missed and duplicate detections for remote objects, which is a common and challenging issue for camera-based methods.

V. CONCLUSION

In this paper, we propose a novel LSS-based multi-view 3D object detection framework, PolarBEVDet. It transforms the multi-view image features into a polar BEV representation instead of a Cartesian BEV representation, which is able to better adapt the image information distribution and can easily preserve the view symmetry. In addition, it also improves the quality of feature extraction by applying 2D auxiliary supervision and spatial attention enhancement in perspective view and BEV, respectively. Extensive experiments validate the effectiveness of these improvements and show that PolarBEVDet achieves remarkable performance. Notably, the polar BEV representation has significant advantages in both near-range perception and robustness of azimuth changes, and porting experiments have also demonstrated its superior universality. Therefore, the polar BEV representation, as a comparable or even superior alternative to the Cartesian BEV representation, holds promise in further motivating future research on the LSS paradigm.

REFERENCES

- [1] B. Wang, H. Zheng, L. Zhang, N. Liu, R. M. Anwer, H. Cholakkal, Y. Zhao, and Z. Li, "BEVRefiner: Improving 3d object detection in bird's-eye-view via dual refinement," vol. 25, no. 10, pp. 15094-15105, 2024.
- [2] C. Shu, J. Deng, F. Yu, and Y. Liu, "3DPPE: 3d point positional encoding for transformer-based multi-camera 3d object detection," in *Int. Conf. Comput. Vis.*, Oct. 2023, pp. 3580-3589.
- [3] H. Li, C. Sima, J. Dai, W. Wang, L. Lu, H. Wang, J. Zeng, Z. Li, J. Yang, H. Deng, H. Tian, E. Xie, J. Xie, L. Chen, T. Li, Y. Li, Y. Gao, X. Jia, S. Liu, J. Shi, D. Lin, and Y. Qiao, "Delving into the devils of bird's-eye-view perception: A review, evaluation and recipe," *IEEE Transactions on Pattern Analysis and Machine Intelligence*, vol. 46, no. 4, pp. 2151-2170, 2024.
- [4] T. Wang, X. Zhu, J. Pang, and D. Lin, "FCOS3D: Fully convolutional one-stage monocular 3d object detection," in *IEEE Conf. Comput. Vis. Worksh.*, Oct. 2021, pp. 913-922.
- [5] D. Park, R. Ambrus, V. Guizilini, J. Li, and A. Gaidon, "Is pseudo-lidar needed for monocular 3d object detection?" in *Int. Conf. Comput. Vis.*, Oct. 2021, pp. 3142-3152.
- [6] C. Reading, A. Harakeh, J. Chae, and S. L. Waslander, "Categorical depth distribution network for monocular 3d object detection," in *IEEE Conf. Comput. Vis. Pattern Recog.*, Jun. 2021, pp. 8555-8564.
- [7] T. Wang, X. Zhu, J. Pang, and D. Lin, "Probabilistic and geometric depth: Detecting objects in perspective," in *Conf. Robot. Learn.*, Dec. 2022, pp. 1475-1485.
- [8] H. Sheng, S. Cai, N. Zhao, B. Deng, M. Zhao, and G. H. Lee, "PDR: Progressive depth regularization for monocular 3d object detection," vol. 33, no. 12, pp. 7591-7603, 2023.
- [9] J. Huang, G. Huang, Z. Zhu, Y. Yun, and D. Du, "BEVDet: High-performance multi-camera 3d object detection in bird-eye-view," *arXiv preprint arXiv:2112.11790*, 2021.
- [10] J. Huang and G. Huang, "BEVDet4D: Exploit temporal cues in multi-camera 3d object detection," *arXiv preprint arXiv:2203.17054*, 2022.
- [11] Y. Li, Z. Ge, G. Yu, J. Yang, Z. Wang, Y. Shi, J. Sun, and Z. Li, "BEVDepth: Acquisition of reliable depth for multi-view 3d object detection," in *AAAI*, vol. 37, Feb. 2023, pp. 1477-1485.
- [12] Z. Li, W. Wang, H. Li, E. Xie, C. Sima, T. Lu, Y. Qiao, and J. Dai, "BEVFormer: Learning bird's-eye-view representation from multi-camera images via spatiotemporal transformers," in *Eur. Conf. Comput. Vis.*, Oct. 2022, pp. 1-18.
- [13] Y. Liu, T. Wang, X. Zhang, and J. Sun, "PETR: Position embedding transformation for multi-view 3d object detection," in *Eur. Conf. Comput. Vis.*, Oct. 2022, pp. 531-548.
- [14] J. Philion and S. Fidler, "Lift, Splat, Shoot: Encoding images from arbitrary camera rigs by implicitly unprojecting to 3d," in *Eur. Conf. Comput. Vis.*, Oct. 2020, pp. 194-210.
- [15] C. Feng, Z. Jie, Y. Zhong, X. Chu, and L. Ma, "Aedet: Azimuth-invariant multi-view 3d object detection," in *IEEE Conf. Comput. Vis. Pattern Recog.*, Jun. 2023, pp. 21580-21588.
- [16] C. Yang, Y. Chen, H. Tian, C. Tao, X. Zhu, Z. Zhang, G. Huang, H. Li, Y. Qiao, L. Lu *et al.*, "BEVFormer v2: Adapting modern image backbones to bird's-eye-view recognition via perspective supervision," in *IEEE Conf. Comput. Vis. Pattern Recog.*, Jun. 2023, pp. 17830-17839.
- [17] S. Wang, X. Jiang, and Y. Li, "Focal-PETR: Embracing foreground for efficient multi-camera 3d object detection," vol. 9, no. 1, pp. 1481-1489, 2024.
- [18] M. Guo, Z. Zhang, L. Jing, Y. He, K. Wang, and H. Fan, "Cyclic refiner: Object-aware temporal representation learning for multi-view 3d detection and tracking," *Int. J. Comput. Vis.*, pp. 1-23, 2024.
- [19] Q. Song, Q. Hu, C. Zhang, Y. Chen, and R. Huang, "Divide and conquer: Improving multi-camera 3d perception with 2d semantic-depth priors and input-dependent queries," *IEEE Trans. Image Process.*, vol. 33, pp. 897-909, 2024.
- [20] Y. Li, H. Bao, Z. Ge, J. Yang, J. Sun, and Z. Li, "BEVStereo: Enhancing depth estimation in multi-view 3d object detection with temporal stereo," in *AAAI*, vol. 37, Feb. 2023, pp. 1486-1494.
- [21] J. Park, C. Xu, S. Yang, K. Keutzer, K. M. Kitani, M. Tomizuka, and W. Zhan, "Time will tell: New outlooks and a baseline for temporal multi-view 3d object detection," in *Int. Conf. Learn. Represent.*, May 2023.
- [22] H. Caesar, V. Bankiti, A. H. Lang, S. Vora, V. E. Liong, Q. Xu, A. Krishnan, Y. Pan, G. Baldan, and O. Beijbom, "nuScenes: A multimodal dataset for autonomous driving," in *IEEE Conf. Comput. Vis. Pattern Recog.*, Jun. 2020, pp. 11621-11631.
- [23] J. Huang and G. Huang, "BEVPoolv2: A cutting-edge implementation of BEVDet toward deployment," *arXiv preprint arXiv:2211.17111*, 2022.
- [24] J. Zhang, Y. Zhang, Q. Liu, and Y. Wang, "SA-BEV: Generating semantic-aware bird's-eye-view feature for multi-view 3d object detection," in *Int. Conf. Comput. Vis.*, Oct. 2023, pp. 3348-3357.
- [25] N. Carion, F. Massa, G. Synnaeve, N. Usunier, A. Kirillov, and S. Zagoruyko, "End-to-end object detection with transformers," in *Eur. Conf. Comput. Vis.*, Oct. 2020, pp. 213-229.

- [26] X. Zhu, W. Su, L. Lu, B. Li, X. Wang, and J. Dai, “Deformable DETR: Deformable transformers for end-to-end object detection,” *arXiv preprint arXiv:2010.04159*, 2020.
- [27] S. Liu, F. Li, H. Zhang, X. Yang, X. Qi, H. Su, J. Zhu, and L. Zhang, “DAB-DETR: Dynamic anchor boxes are better queries for DETR,” in *Int. Conf. Learn. Represent.*, May. 2022.
- [28] Y. Wang, V. C. Guizilini, T. Zhang, Y. Wang, H. Zhao, and J. Solomon, “DETR3D: 3d object detection from multi-view images via 3d-to-2d queries,” in *Conf. Robot. Learn.*, Dec. 2022, pp. 180–191.
- [29] Y. Liu, J. Yan, F. Jia, S. Li, A. Gao, T. Wang, and X. Zhang, “PETRv2: A unified framework for 3d perception from multi-camera images,” in *Int. Conf. Comput. Vis.*, Oct. 2023, pp. 3262–3272.
- [30] D. Chen, J. Li, V. Guizilini, R. A. Ambrus, and A. Gaidon, “Viewpoint equivariance for multi-view 3d object detection,” in *IEEE Conf. Comput. Vis. Pattern Recog.*, Jun. 2023, pp. 9213–9222.
- [31] K. Xiong, S. Gong, X. Ye, X. Tan, J. Wan, E. Ding, J. Wang, and X. Bai, “CAPE: Camera view position embedding for multi-view 3d object detection,” in *IEEE Conf. Comput. Vis. Pattern Recog.*, Jun. 2023, pp. 21570–21579.
- [32] S. Wang, Y. Liu, T. Wang, Y. Li, and X. Zhang, “Exploring object-centric temporal modeling for efficient multi-view 3d object detection,” in *Int. Conf. Comput. Vis.*, Oct. 2023, pp. 3621–3631.
- [33] H. Liu, Y. Teng, T. Lu, H. Wang, and L. Wang, “SparseBEV: High-performance sparse 3d object detection from multi-camera videos,” in *Int. Conf. Comput. Vis.*, Oct. 2023, pp. 18580–18590.
- [34] Y. Zhang, Z. Zhou, P. David, X. Yue, Z. Xi, B. Gong, and H. Foroosh, “PolarNet: An improved grid representation for online lidar point clouds semantic segmentation,” in *IEEE Conf. Comput. Vis. Pattern Recog.*, Jun. 2020, pp. 9601–9610.
- [35] Z. Zhou, Y. Zhang, and H. Foroosh, “Panoptic-PolarNet: Proposal-free lidar point cloud panoptic segmentation,” in *IEEE Conf. Comput. Vis. Pattern Recog.*, Jun. 2021, pp. 13194–13203.
- [36] X. Zhu, H. Zhou, T. Wang, F. Hong, Y. Ma, W. Li, H. Li, and D. Lin, “Cylindrical and asymmetrical 3d convolution networks for LiDAR segmentation,” in *IEEE Conf. Comput. Vis. Pattern Recog.*, Jun. 2021, pp. 9939–9948.
- [37] F. Hong, H. Zhou, X. Zhu, H. Li, and Z. Liu, “LiDAR-based panoptic segmentation via dynamic shifting network,” in *IEEE Conf. Comput. Vis. Pattern Recog.*, Jun. 2021, pp. 13090–13099.
- [38] Q. Chen, S. Vora, and O. Beijbom, “PolarStream: Streaming object detection and segmentation with polar pillars,” *Adv. Neural Inform. Process. Syst.*, vol. 34, pp. 26871–26883, Dec. 2021.
- [39] M. Nie, Y. Xue, C. Wang, C. Ye, H. Xu, X. Zhu, Q. Huang, M. B. Mi, X. Wang, and L. Zhang, “PARTNER: Level up the polar representation for lidar 3d object detection,” in *Int. Conf. Comput. Vis.*, Oct. 2023, pp. 3801–3813.
- [40] Z. Liu, S. Chen, X. Guo, X. Wang, T. Cheng, H. Zhu, Q. Zhang, W. Liu, and Y. Zhang, “Vision-based uneven BEV representation learning with polar rasterization and surface estimation,” in *Conf. Robot. Learn.*, Nov. 2023, pp. 437–446.
- [41] S. Chen, X. Wang, T. Cheng, Q. Zhang, C. Huang, and W. Liu, “Polar parametrization for vision-based surround-view 3d detection,” *arXiv preprint arXiv:2206.10965*, 2022.
- [42] Y. Jiang, L. Zhang, Z. Miao, X. Zhu, J. Gao, W. Hu, and Y.-G. Jiang, “PolarFormer: Multi-camera 3d object detection with polar transformer,” in *AAAI*, vol. 37, Feb. 2023, pp. 1042–1050.
- [43] X. Lin, T. Lin, Z. Pei, L. Huang, and Z. Su, “Sparse4D: Multi-view 3d object detection with sparse spatial-temporal fusion,” *arXiv preprint arXiv:2211.10581*, 2022.
- [44] T. Yin, X. Zhou, and P. Krahenbuhl, “Center-based 3d object detection and tracking,” in *IEEE Conf. Comput. Vis. Pattern Recog.*, Jun. 2021, pp. 11784–11793.
- [45] X. Li, W. Wang, L. Wu, S. Chen, X. Hu, J. Li, J. Tang, and J. Yang, “Generalized focal loss: Learning qualified and distributed bounding boxes for dense object detection,” *Adv. Neural Inform. Process. Syst.*, vol. 33, pp. 21002–21012, Dec. 2020.
- [46] Z. Tian, C. Shen, H. Chen, and T. He, “FCOS: Fully convolutional one-stage object detection,” in *Int. Conf. Comput. Vis.*, Oct. 2019, pp. 9627–9636.
- [47] H. Rezatofighi, N. Tsoi, J. Gwak, A. Sadeghian, I. Reid, and S. Savarese, “Generalized intersection over union: A metric and a loss for bounding box regression,” in *IEEE Conf. Comput. Vis. Pattern Recog.*, Jun. 2019, pp. 658–666.
- [48] H. Law and J. Deng, “Cornernet: Detecting objects as paired keypoints,” in *Eur. Conf. Comput. Vis.*, Sep. 2018, pp. 734–750.
- [49] Z. Li, Z. Yu, W. Wang, A. Anandkumar, T. Lu, and J. M. Alvarez, “FB-BEV: BEV representation from forward-backward view transformations,” in *Int. Conf. Comput. Vis.*, Oct. 2023, pp. 6919–6928.
- [50] C. Han, J. Yang, J. Sun, Z. Ge, R. Dong, H. Zhou, W. Mao, Y. Peng, and X. Zhang, “Exploring recurrent long-term temporal fusion for multi-view 3d perception,” *IEEE Rob. Autom. Lett.*, vol. 9, no. 7, pp. 6544–6551, 2024.
- [51] I. Loshchilov and F. Hutter, “Decoupled weight decay regularization,” *arXiv preprint arXiv:1711.05101*, 2017.
- [52] K. He, X. Zhang, S. Ren, and J. Sun, “Deep residual learning for image recognition,” in *IEEE Conf. Comput. Vis. Pattern Recog.*, Jun. 2016, pp. 770–778.
- [53] Y. Lee, J.-w. Hwang, S. Lee, Y. Bae, and J. Park, “An energy and gpu-computation efficient backbone network for real-time object detection,” in *IEEE Conf. Comput. Vis. Pattern Recog. Worksh.*, Jun. 2019, pp. 752–760.
- [54] J. Deng, W. Dong, R. Socher, L. Li, K. Li, and F. Li, “Imagenet: A large-scale hierarchical image database,” in *IEEE Conf. Comput. Vis. Pattern Recog.*, Jun. 2009, pp. 248–255.
- [55] B. Zhu, Z. Jiang, X. Zhou, Z. Li, and G. Yu, “Class-balanced grouping and sampling for point cloud 3d object detection,” *arXiv preprint arXiv:1908.09492*, 2019.
- [56] Z. Liu, H. Mao, C.-Y. Wu, C. Feichtenhofer, T. Darrell, and S. Xie, “A convnet for the 2020s,” in *IEEE Conf. Comput. Vis. Pattern Recog.*, Jun. 2022, pp. 11976–11986.